Journal Pre-proofs

Hydrogel-immobilized nanotherapeutics: Inhibition of protective autophagy to amplify STING for postsurgical tumor immunotherapy

Hong Wang, Weikai Sun, Dawei Zhou, Yafei Qi, Zhiliang Gao, Jiwei Cui, Dexin Yu

PII: S1385-8947(23)06943-7
DOI: https://doi.org/10.1016/j.cej.2023.148211
Reference: CEJ 148211

To appear in: *Chemical Engineering Journal*

Received Date: 28 September 2023
Revised Date: 2 December 2023
Accepted Date: 18 December 2023

Please cite this article as: H. Wang, W. Sun, D. Zhou, Y. Qi, Z. Gao, J. Cui, D. Yu, Hydrogel-immobilized nanotherapeutics: Inhibition of protective autophagy to amplify STING for postsurgical tumor immunotherapy, *Chemical Engineering Journal* (2023), doi: https://doi.org/10.1016/j.cej.2023.148211

Hydrogel-immobilized nanotherapeutics: inhibition of protective autophagy to amplify STING for postsurgical tumor immunotherapy

Hong Wang [a,c], Weikai Sun [a,c], Dawei Zhou [a,c], Yafei Qi [a,c], Zhiliang Gao [a,b,*], Jiwei Cui [b,*], Dexin Yu [a,*]

[a] *Department of Radiology, Qilu Hospital of Shandong University, Jinan, Shandong 250012, China.*

[b] *Key Laboratory of Colloid and Interface Chemistry of the Ministry of Education, School of Chemistry and Chemical Engineering, Shandong University, Jinan, Shandong 250100, China.*

[c] *Laboratory of Basic Medical Sciences, Qilu Hospital of Shandong University, Jinan, Shandong, 250012, China.*

* Corresponding author.

E-mail addresses: zlgao@sdu.edu.cn (Z. Gao), jwcui@sdu.edu.cn (J. Cui), yudexin0330@sina.com (D. Yu).

Abstract

Activating the inherent stimulator of Active Ingredient gene (STING) pathway of cancer cells can inhibit tumor growth but can also induce protective autophagy of tumor cells to inhibit the STING-mediated immunotherapy. Therefore, amplification of STING activation and inhibition of autophagy could potentiate the cancer immunotherapy. Here, hydrogel-immobilized nanoparticles loaded with glucose oxidase (GOx), manganese ions (Mn^{2+}) and Active Ingredient (HCQ) are prepared at the postsurgical site to enhance cancer therapy *via* activating the STING pathway and regulating the autophagy pathway. The delivered GOx and Mn^{2+} exert a chemo-dynamic therapy (CDT) to induce dsDNA damage, which can further initiate the STING pathway. HCQ can effectively inhibit protective autophagy associated with STING pathway activation, further amplify the antitumor immune responses. The synergistic delivery of CDT agents (*i.e.*, GOx and Mn^{2+}), STING agonists (*i.e.*, Mn^{2+}) and autophagy inhibitors (*i.e.*, HCQ) results in a specific immune response, significantly inhibit tumor recurrence and metastatic tumor growth, which could extend the survival rate of mice suffered from the triple-negative breast cancer (TNBC).

Keywords: chemodynamic therapy, autophagy inhibition, STING pathway, tumor immunotherapy, tumor recurrence

1. Introduction

Surgical resection is the main clinical treatment strategy for tumor therapy (*e.g.*, triple-negative breast cancer, TNBC) while it faces the challenges of recurrence and metastasis.[1, 2]Regarding tumor recurrence and metastasis, chemotherapy and radiotherapy are the most commonly used methods, but these methods are often useless in suppressing the growth of distant metastases and are usually associated with severe side effects or damage to the immune system.[3-7] Immunotherapy that relies on the host's own immune system to trigger anticancer immune responses has received widespread attention.[8-11] However, insufficient postoperative infiltration of proinflammatory immune cells and a suppressed "cold" tumors immune microenvironment limit the application of immunotherapy.[10, 12-15] Therefore, transforming immune "cold" tumors into immune "hot" tumors and ameliorating the inhibitory tumor microenvironment (TME) are the keys to enhancing the anti-tumor immune responses and inhibiting of recurrent metastases after surgery for TNBC.[16]

Activating the stimulator of Active Ingredient gene (STING) pathway can not only induce immune response in antiviral and antibacterial therapy but also in antitumor therapy, as well as in reversing the tumor-suppressive microenvironment, *i.e.*, converting "cold" tumors to "hot" tumors.[17-21] For example, cyclic GMP-AMP synthase (cGAS) in tumor cells senses intracellular damaged DNA, activates STING pathway and upregulates type I Active Ingredients (IFN-β), which subsequently reverse the TME by promoting the maturation of dendritic cells (DCs) and recruiting $CD8^+$ T cells to improve immunotherapy efficacy.[22,23] Recent studies have demonstrated that Mn^{2+} can effectively enhance the sensitivity of cGAS to dsDNA and amplify the activation of the STING pathway.[24-27] In addition, the binding of Mn^{2+} enhances the binding affinity of STING and cGAMP, which hyperactivates STING pathway in respond to cytosolic DNA. [28]

Meanwhile, in response to the activation of the STING signaling pathway, tumor cells also trigger their internal protective autophagy. [29,30] As a conserved cellular protection mechanism, autophagy maintains homeostasis by sequestering cytoplasmic components in autophagosomes and delivering them to lysosomes for degradation and recycling into metabolic substrates. In addition, autophagy clears damaged dsDNA induced by oxidative stress, which may attenuate downstream chaining effects such as STING. [31-35] Autophagy negatively regulates the STING pathway, which acts as a "brake" signal on STING to avoid excessive immunity.[36] Inspired by this, inhibiting autophagy can amplify the activation of the STING pathway and improve tumor immunotherapy.

Herein, we report the engineering of hydrogel-immobilized nanoparticles (NPs) to deliver Mn^{2+}, glucose oxidase (GOx) and the autophagy inhibitor of Active Ingredient (HCQ) to the postsurgical site for the prevention of TNBC recurrence and inhibition of metastatic tumor growth. GOx is encapsulated into mesoporous silica NPs, followed by coating with metal-phenolic networks (MPNs) of tannic acid and Mn^{2+} (GM@MSN) while HCQ is loaded into liposomes (LipHCQ), both of which are immobilized by hydrogels (H/GM@Gel) (**Scheme 1**a). Mn^{2+} released from the delivery system can activate the STING pathway. Meanwhile, intracellular glucose is oxidized by the delivered GOx to generate H_2O_2, which is further

converted to the toxic •OH in the presence of Mn^{2+}. [37] The produced •OH can not only exert a chemodynamic therapy (CDT) effect, but also induce immunogenic cell death (ICD), which effectively releases tumor antigens and helps to activate specific antitumor immunity.[38] In addition, DNA damage caused by CDT can further activate the STING pathway, which induces DC maturation and stimulates an increase in IFN-β secretion to recruit more effector T cells into the TME. [28,39] Importantly, HCQ inhibits the protective autophagy generated by activating the STING pathway, which relieves the "brake" signal of autophagy and improves the immunotherapy effect (**Scheme 1**b). This work highlights the regulation of the STING pathway and autophagy pathway to enhance antitumor immunity, which could improve tumor immune microenvironments against tumor recurrence and metastatic tumor growth.

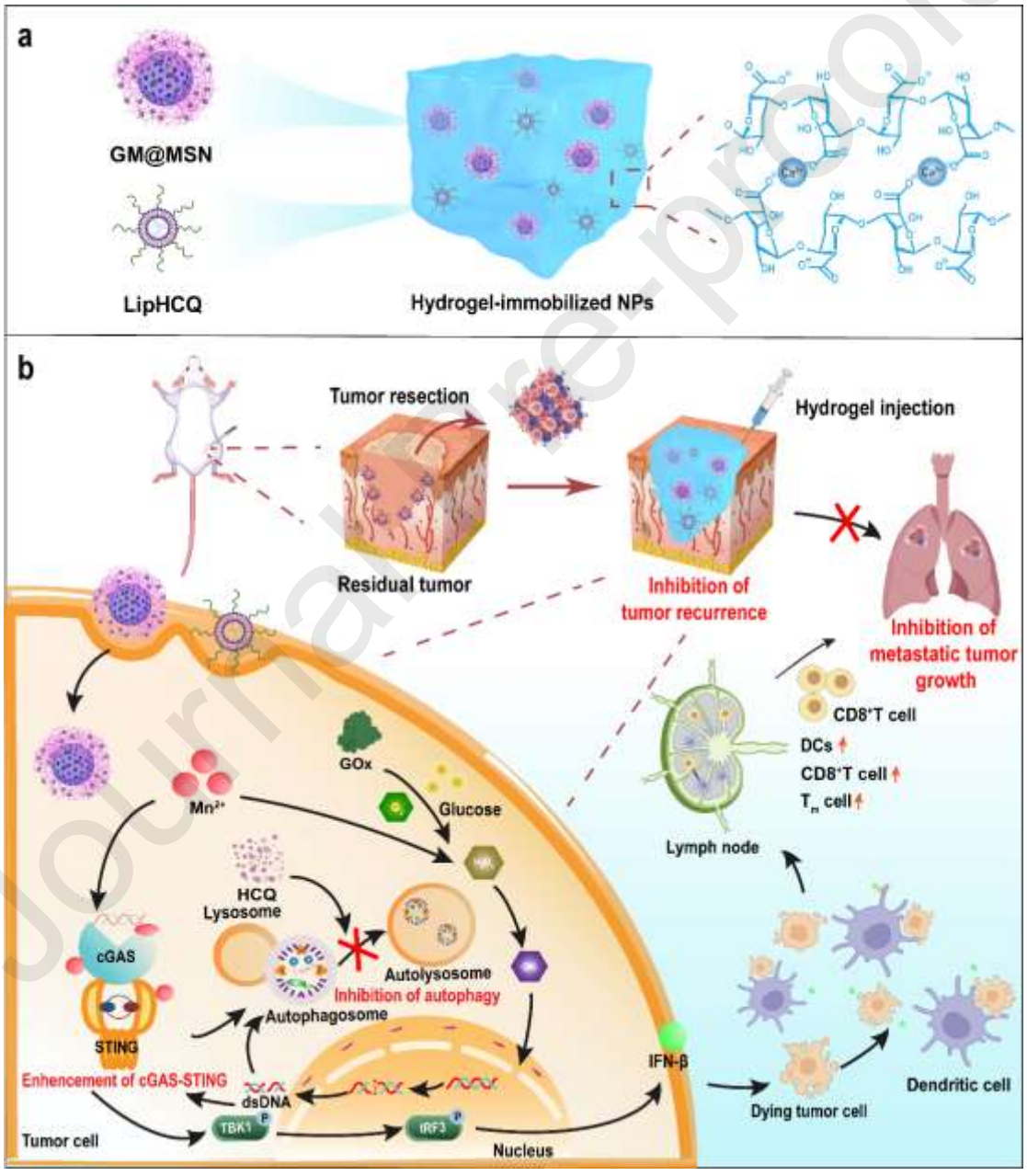

Scheme 1. Schematic synthesis of hydrogel-immobilized NPs and their biological functions. a) Fabrication of hydrogel-immobilized NPs loaded with therapeutics. b) Application of hydrogel-immobilized NPs for activating the STING pathway against TNBC tumor recurrence and metastatic tumor growth. After cellular uptake of GM@MSN and LipHCQ, glucose is converted into gluconic acid and H_2O_2 by GOx. Subsequently, the increased H_2O_2 is converted to •OH in the presence of Mn^{2+}. Meanwhile, CDT-enhanced Mn^{2+} activates the STING pathway with HCQ-inhibited autophagy due to STING activation, which leads to IFN-β released and further promotes DC maturation to induce potent antitumor immunity.

2. Materials and methods

2.1. Preparation of manganese-based NPs

Preparation of MSN-NH_2. MSN (110 nm, 130 mg) was dispersed with 3.9 mL of anhydrous ethanol and washed with anhydrous ethanol three times. Subsequently, 216 μL of $NH_3 \cdot H_2O$ and 130 μL of 3-aminopropyltriethoxysilane (APTES) were added to the suspension, which was stirred for 12 h. The products were each washed with ethanol and water three times. Finally, the MSN-NH_2 were distributed in water for further use.

Preparation of GM@MSN. For the encapsulation of GOx, MSN-NH_2 (20 mg) dispersion was incubated with 1.2 mg of GOx for 6 h at 4 ℃, followed by centrifugation to remove the unencapsulated GOx. The obtained GOx-loaded MSNs (G@MSN) were dispersed in 20 mL of water. Subsequently, 0.2 mL of TA (40 mg/mL), 0.2 mL of $MnCl_2 \cdot 4H_2O$ (7.3 mg/mL) and 20 mL of MOPS (20 mM, pH 7.4) were added sequentially to form the MPN coatings. MPNs coated amineo group-functionalized MSN was set as the control group (M@MSN). Finally, the GOx- and Mn^{2+}-loaded MSN (GM@MSN) were incubated with BSA (1 mg/mL, 5 mL) to form the BSA corona.

Preparation of LipHCQ. LipHCQ was prepared by a transmembrane ammonium sulfate gradient method. In brief, HSPC (75 mg), Chol (25 mg), and DSPE-mPEG2000 (25 mg) were dissolved in 10 mL of chloroform. A lipid film was formed by removing the solvent with a rotary evaporator. Then, 10 mL of ammonium sulfate solution (0.3 M) was added for rehydration and the liposomes were sequentially extruded through the high-pressure microfluidizer (NanoGenizer-II, Genizer) four times at an operation pressure of 15000 psi. The obtained liposomes were dialyzed with PBS buffer (10 mM) for 24 h and incubated with 15 mg of HCQ (60 °C) for 30 min, followed by centrifugation (50000 g 40 min, 4 °C) to remove the free HCQ.

2.2. Fabrication of the hydrogel-immobilized NPs

Sodium alginate (ALG, 50 mg) was added into 5 mL water and stirred for 12 h to obtain a clear solution. Then, GM@MSN together with LipHCQ (H/GM@MSN) were added to the above alginate solution. The mixture was stirred vigorously for 2 h. Finally, the mixture was injected into the postsurgical site to form the hydrogel-immobilized NPs which H/GM@MSN-loaded hydrogel (H/GM@Gel) with endogenous Ca^{2+}.

2.3. Release and biocompatibility of the hydrogel *in vivo*

To investigate the *in vivo* release of NPs from the hydrogel, Cy5.5-labelled GM@MSN-loaded hydrogel (GM@Gel) was applied to fabricate hydrogel-immobilized NPs in the postsurgical site. Performed fluorescence imaging using the IVIS Spectrum imaging system (PerkinElmer, USA) at the predetermined time points. Fluorescence (excitation of 675nm, and emission of 694nm).

To assess the biosafety of hydrogels, skin and muscle tissues from the hydrogel injection site was collected after 14 days for further H&E analysis.

2.4. Cytotoxicity of therapeutics-loaded NPs

CCK-8 assay. In vitro cytotoxicity was evaluated using the Cell Counting Kit-8 (CCK-8) assay of different NPs against 4T1 cells. 4T1 tumor cells (9×10^3 per well) were plated in 96-well plates and incubated in a cell incubator for 24 h. LipHCQ, M@MSN, GM@MSN and H/GM@MSN (equivalent GOx concentration of 0.391, 0.781, 1.563, 3.125 and 6.250 μg/mL; equivalent Mn^{2+} concentration of 1.173, 2.343, 4.689, 9.375 and 18.750 μg/mL) were incubated with cells for 24 h. Subsequently, cell viability was then assessed by adding CCK-8 solution to each well. (absorbance at 450 nm).

Live/dead assay. 4T1 cells were seeded in 24-well plates at 1×10^5 cells/well and cultured in a cell incubator for 12 h. After treatment with LipHCQ, M@MSN, GM@MSN and H/GM@MSN (GOx, 0.6 μg/mL; Mn^{2+}, 1.8 μg/mL; HCQ, 10 μg/mL), Calcein-AM (2 μM) and PI (4 μM) solutions were added to stain live cells and dead cells, respectively. Cells were imaged by using a fluorescence microscope.

Cell apoptosis. 2×10^5 cells/well were plated into 6-well plates and cultured in a cell incubator for 24 h. Subsequently, 4T1 cells were treated with LipHCQ, M@MSN, GM@MSN and H/GM@MSN (GOx, 0.6 μg/mL; Mn^{2+}, 1.8 μg/mL; HCQ, 10 μg/mL) for 24 h. Cells were digested with EDTA-free trypsin, centrifuged to discard the supernatant and collected, washed twice with pre-cooled PBS, 100 μl of 1 × Binding Buffer was added and gently blown to a single-cell suspension. 5 μl Annexin V-FITC and 5 μl PI staining solution were added and incubated at 25 °C for 10 min for staining. The stained samples were detected by flow cytometry within 1 h.

2.5. Monitoring of cellular autophagy

Cells were inoculated in 6-well plates at a density of 3×10^5 cells/well. After 24 h, incubation of cells with LipHCQ, M@MSN, GM@MSN and H/GM@MSN, respectively (GOx, 0.8 μg/mL; Mn^{2+}, 2.4 μg/mL) for 24 h. Then collecting cells with a spatula and fixed at 4 °C for 1 h with an electron microscope fixative. After fixation, dehydration, sectioning, staining and other operations, autophagosomes were observed by Bio-TEM.

2.6. *In vivo* antitumor efficacy

To verify the anti-recurrence and inhibit metastatic tumor growth effect of H/GM@Gel, a postoperative breast tumor model was established. 90% of the primary tumor was resected when the tumor volume reached approximately 100-150 mm^3. Following surgery, mice were then randomised into 5 groups and different hydrogel-immobilized NPs of 100 μL were injected into the operation area, including PBS, LipHCQ@Gel (H@Gel), M@Gel, GM@Gel, H/GM@Gel (GOx, 3 mg/kg; Mn^{2+}, 1.2 mg/kg; HCQ, 10 mg/kg). Every 3 days, body weight and recurrent tumor volume were measured and the tumor sizes were calculated according to the following equation: volume (mm^3) = 0.5×$width^2$ (mm^2) × length (mm). On day 24, tumors were harvested for further analysis. Specifically, H&E and immunohistochemically staining of tumor tissues were used for investigate the necrosis and proliferation of tumor cells. It also included the autophagy proteins expression of LC3 and p62 in tumor tissue. In addition, immunofluorescence staining assay was used for further analysis of $CD4^+$ and $CD8^+$ T cells and P-STING (Ser 366) proteins.

2.7. Lung metastatic analysis

To establish the metastatic lung tumor models, primary tumor model was constructed using the method described above. At day 8, 4T1 cells (1×10^5) were intravenously injected into mice. After resection, mice were randomly divided into five groups for treatment as above. After end of treatment, the survival curve and lung tissue pictures of mice were obtained. The metastatic lesions in lungs were recorded and sectioned for H&E analysis.

2.8. Flow cytometry analysis

To evaluate the improvement of tumor immune microenvironment, inguinal lymph nodes and the tumor tissues were collected to analyse the anti-tumor immune response using a FACS Calibur flow cytometer. The tissues obtained were minced and homogenised into a single-cell suspension using a 40 μm-cell strainer. After lysing erythrocytes, T cells were stained with FITC-CD3ε, APC-CD4, PE-CD8, PE-Foxp3, PE/Cyanine7-CD25, APC-CD44, FITC-CD62L antibodies. Cells were stained with APC-CD11c, FITC-CD80 and PE/Cyanine7-CD86 monoclonal antibodies to analyse DCs in tumor and lymph nodes. Meanwhile, FITC-CD45, PE-CD11b, APC-Gr1 monoclonal antibodies were used for MDSC cells analysis.

2.9. Statistical analysis

The data were expressed as mean ± SD, and statistical comparisons between two groups were conducted using unpaired Student's t-tests while three or more groups are conducted using one-way ANOVA and Tukey multiple comparison tests. *P* values considered statistically significant were less than 0.05 (**P* <0.05, ***P* < 0.01, ****P* < 0.001, *****P* < 0.0001). All statistical analysis were carried out using GraphPad Prism (Version 6.01).

3. Results and discussion

3.1. Preparation and characterization of therapeutics-loaded NPs

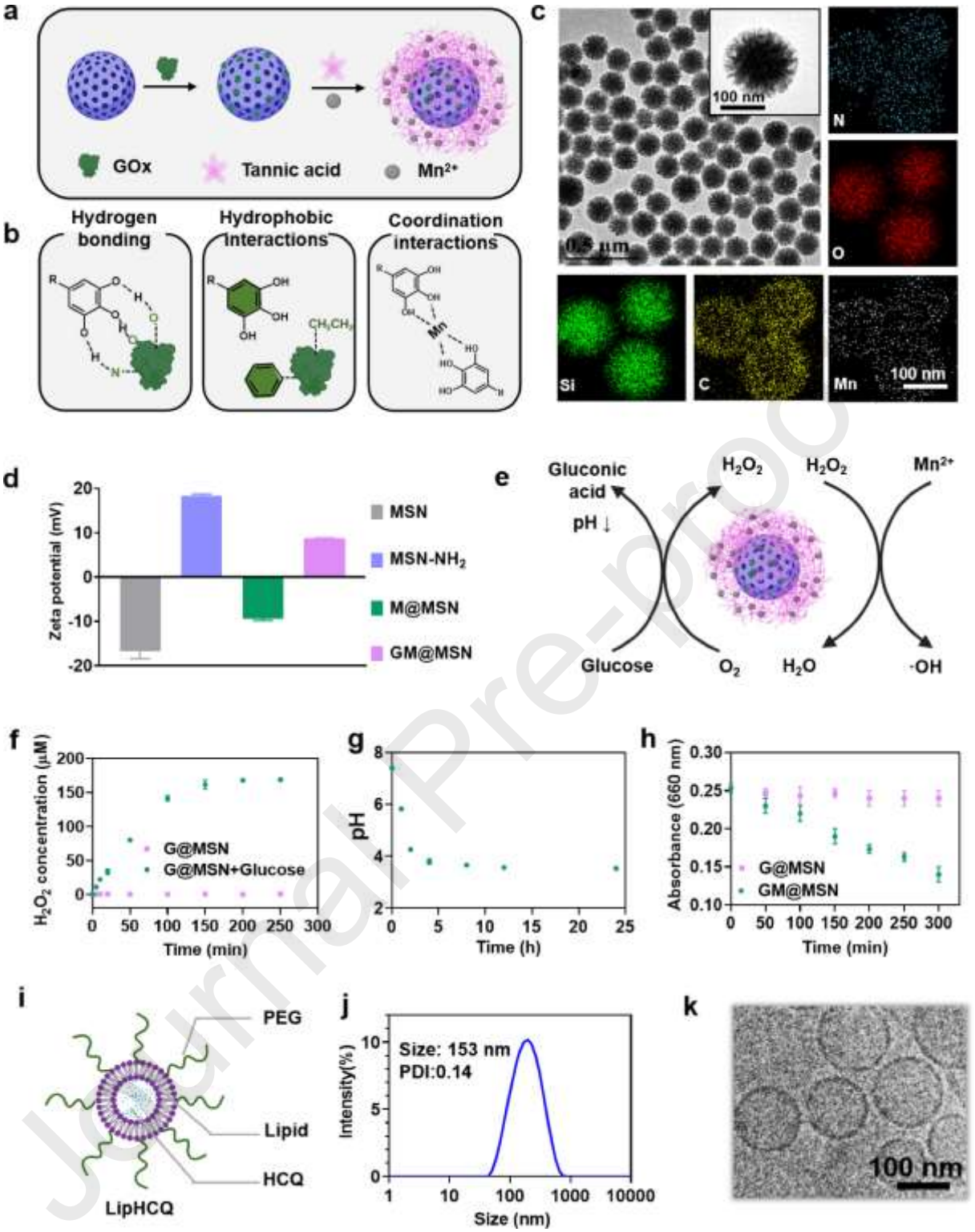

Figure 1. Preparation and characterization of NPs. a) Schematic to illustrate how to prepare the following GM@MSN NP. b) Driving forces for the fabrication of GM@MSN, which include coordination interactions, hydrophobic interactions, and hydrogen bonds. c) TEM images and EDX mapping photographs of GM@MSN. d) Zeta potentials of MSN, MSN-NH_2, M@MSN, GM@MSN. e) Schematic diagram of GOx-catalyzed glucose and Fenton-like reactions. f) H_2O_2 concentration and g) pH changes during the catalytic reaction process. h) MB degradation

behavior in the presence of G@MSN and GM@MSN. i) Structure of the LipHCQ. j) Size distribution of LipHCQ. k) Cryo-TEM images of LipHCQ.

GM@MSN were prepared by using a two-step method (**Figure 1**a). GOx was first loaded into amino group-functionalized MSN (G@MSN) **(Figure S1**) (surface area: 1430.2 m^2/g; pore size: 15.7 nm), driven by the electrostatic interactions between negatively charged GOx and positively charged amine-functionalized MSN. Subsequently, Mn^{2+} was loaded on the surface of G@MSN, mediated by the formation of MPNs. MPNs coated amino group-functionalized MSN (M@MSN) was set as the control group. The coating of MPNs could be driven by multiple intermolecular interactions, including coordination interactions, hydrophobic interactions, and hydrogen bonds (**Figure 1**b). There were no significant changes in the morphology of the NPs after each modification step, as shown in **Figures S2** and **S3**, indicating the good monodispersity of MSN (~150 nm). The successful construction of GM@MSN was confirmed by EDX mapping and ζ-potential results confirm the (**Figures 1**c, d). The loading levels of GOx and Mn^{2+} were 1% and 3%, respectively. It has been reported that GOx was able to catalyse glucose to produce gluconic acid and H_2O_2 in the tumor. In the presence of Mn^{2+}, the resulting H_2O_2 can be converted by a Fenton-like reaction into the highly toxic •OH (**Figure 1**e). [40,41] To detect the production of H_2O_2, G@MSN were incubated with glucose in the presence of ammonium titanium oxalate, and the concentration of H_2O_2 increased over time (**Figures 1**f and **S4**). In addition, the solution pH also gradually decreased because of the production of gluconic acid (**Figure 1**g). Methylene blue (MB) degradation experiments demonstrated the production of •OH. The occurrence of Fenton-like reactions was confirmed by a significant reduction in the absorption of MB in the GM@MSN group, as shown in **Figure 1**h. LipHCQ was prepared by a film-dispersion method (**Figure 1**i). As shown in **Figures 1**j and **S5**, the average size of LipHCQ was ~150 nm and the ζ-potential were approximately -25 mV. The hollow vesicle structures of the liposomes were confirmed by the results of the cryo-transmission electron microscopy (cryo-TEM) (**Figure 1**k). The loading content of HCQ in liposomes was 10.7% (**Figure S6**). In addition, the size of the LipHCQ and GM@MSN NPs did not significantly change after incubation with water or culture medium, indicating their good stability *in vitro* (**Figure S7**).

3.2. Preparation and characterization of the hydrogel-immobilized NPs.

The hydrogel-immobilized NPs were in situ assembled by the injection of alginate (ALG) solution containing GM@MSN and LipHCQ into the tumor postsurgical site, which could be subsequently cross-linked by the Ca^{2+} and formed hydrogel networks (**Figures 2**a, **S8**). Scanning electron microscopy (SEM) images show the porous structure of the hydrogel-immobilized NPs (**Figure 2**b). Enlarged SEM images and CLSM results indicated the homogeneous distribution of NPs in the hydrogel (**Figures 2**c, d). Dynamic stress sweep rheological tests were performed to investigate the mechanical strength of ALG hydrogels. **Figure S9** shows that the yield stress (ranging from 20 to 300 Pa) and storage modus (G') (ranging from 13000 to 60000 Pa) increased gradually with the increase in Ca^{2+} concentration. Moreover, the introduction of NPs into hydrogels can enhance the mechanical strength of the hydrogels, which was attributed to the strong hydrogen bonding between ALG and MPNs (**Figures S10, S11**). In addition, we also study the *in vivo* gelation time. A mixture of

GM@MSN NPs and sodium alginate was injected into mice, and gel samples were collected at the designated time point for rheological testing. From the results, the hydrogel was formed within 15 min after injection *in vivo* **(Figure S12).** An *in vivo* fluorescence imaging system (IVIS) was used to visualize the degradation behavior of the hydrogel-immobilized NPs. As shown in **Figures 2**e, f, approximately 40% of the hydrogel-immobilized NPs can be retained where injected after 7 days, indicating the sustained-release ability of the hydrogel-immobilized NPs. To further validate the *in vivo* biocompatibility and biosafety of the hydrogels, skin and muscle tissues were collected from the hydrogel injection site. As shown in **Figure S13**, no obvious inflammation, edema, tissue necrosis or cell morphology changes were observed at the injection site at 14 days after injection, indicating that the hydrogel had good biocompatibility.

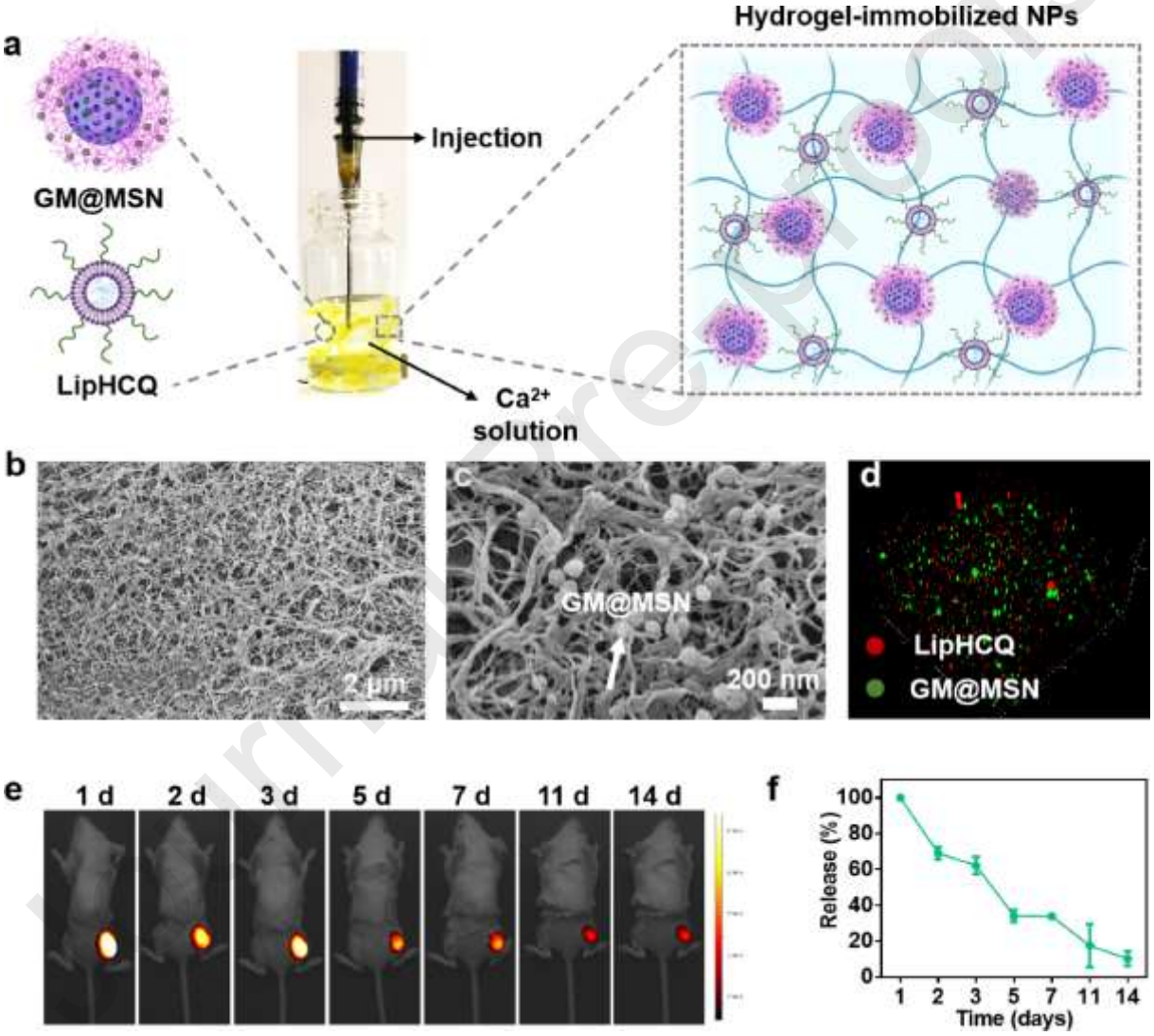

Figure 2. Characterization of the hydrogel-immobilized NPs. a) Schematic illustration of hydrogel-immobilized NPs preparation. b, c) Representative SEM and d) CLSM images of the hydrogels loaded with GM@MSN and LipHCQ. e) Representative fluorescence images and (f) analysis of the Cy5.5-labeled GM@Gel after injection at the postsurgical site.

3.3. Cytotoxicity Evaluation and DC maturation

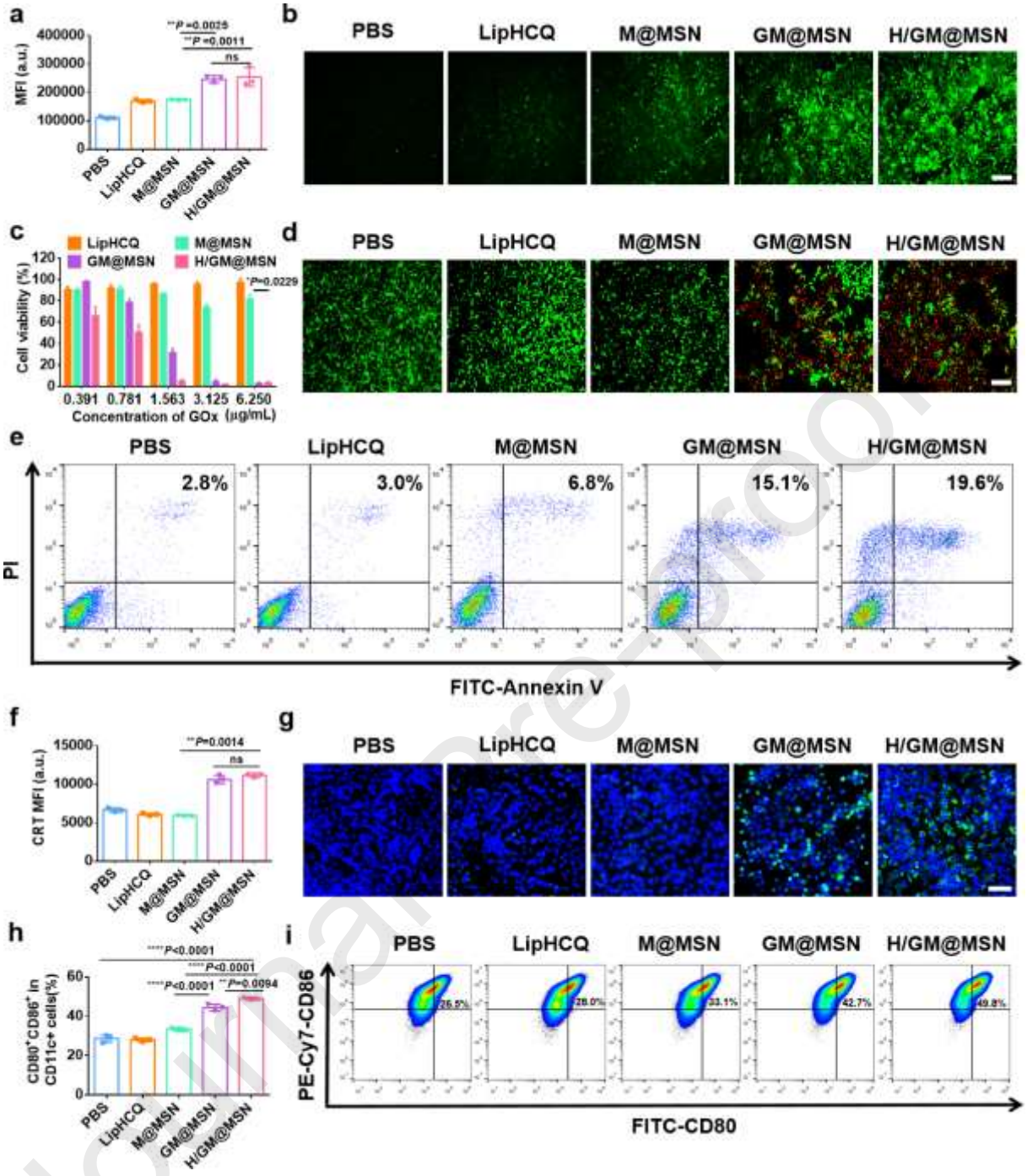

Figure 3. *In vitro* cytotoxicity assay and DC maturation. a) MFI obtained after incubating with PBS, LipHCQ, M@MSN, GM@MSN, and H/GM@MSN for 8 h. b) After different treatments for 8 h fluorescence images of 4T1 cells followed by staining with 10 μM DCFH-DA probe. Scale bar is 100 μm. c) 4T1 cell activity after various treatments at different concentrations of GOx (0.391, 0.781, 1.563, 3.125 and 6.250 μg/mL) (n = 3). d) Fluorescence images of 4T1 cells stained with calcein-AM (green, viable) and PI (red, dead) treated with PBS, LipHCQ, M@MSN, GM@MSN, and H/GM@MSN (GOx: 0.6 μg/mL; Mn^{2+}: 1.8 μg/mL; HCQ: 10 μg/mL). Scale bar is 100 μm. e) Annexin V/PI assay for the evaluation of 4T1 cell apoptosis. CRT expression by f) Flow cytometric analyses and g) immunofluorescence images in 4T1 cells.

Scale bar is 100 μm. h, i) Analyses of DC maturation ($CD80^+CD86^+$ gated on $CD11c^+$) with different treatment. Significant differences were assessed using one-way ANOVA. Data are presented as the mean ± SD (n=3). *$P < 0.05$, **$P < 0.01$, ***$P < 0.001$, ****$P < 0.0001$.

For evaluation of the antitumor activity of GM@MSN together with LipHCQ (H/GM@MSN) *in vitro*, 4T1 cells were incubated with NPs and stained with DAPI and LysoTracker Red probes. The fluorescence intensity increased along with the increase in incubation time, which indicates that more NPs were internalized by cells (**Figure S14**). Further studies revealed that few NPs could interact with the cells after 2 h incubation, suggesting that the cells were just beginning to phagocytose the NPs (**Figure S15**). A 2′,7′-dichlorofluorescin diacetate (DCFH-DA) probe was used to assess ROS production in 4T1 cells to explore the therapeutic mechanism of H/GM@MSN by flow cytometry. The mean fluorescence intensity (MFI) of the M@MSN was weak, while that of the H/GM@MSN group was the highest. Notably, GM@MSN and H/GM@MSN groups were not significantly different, which was because GOx mainly contributed to the ROS production (F=40.39) (**Figure 3**a). Fluorescence microscopy was used to observe the ROS signals in cells after the treatments with LipHCQ, M@MSN, GM@MSN, and H/GM@MSN groups was observed by fluorescence microscopy, which were similar to the results obtained by flow cytometry (**Figure 3**b). The ROS generation resulted from the cascade catalytic reaction in the presence of GOx and Mn^{2+} (**Figure 1**e). [42,43] Moreover, cell cytotoxicity was assessed by a CCK-8 assay *in vitro*. As shown in **Figure 3**c, M@MSN and LipHCQ groups showed negligible cytotoxicity due to the lack of GOx, whereas GM@MSN and H/GM@MSN exhibited dose-dependent cytotoxicity to 4T1 cells. The IC50 values of GOx in the M@MSN and H/GM@MSN groups were 1.15 and 0.94 μg/mL, respectively. As expected, HCQ inhibited internal autophagy and enhanced the STING pathway for a higher killing effect in the H/GM@MSN group. Meanwhile, fibroblast cells (3T3) were used to evaluate the cytocompatibility of the vectors. The MSNs, Lipsomes, and hydrogels exhibited good cytocompatibility at a concentration of 62.5 to 500 μg/mL with a cell viability above 90%, (**Figure S16**). The cytotoxicity of these NPs was also evaluated by live/dead assay. Positive calcein-AM staining (green signal) represents live cells, while positive propidium iodide staining (PI, red signal) indicates dead cells. The cells were mostly alive after incubation with M@MSN, indicating the low toxicity of M@MSN. However, nearly 90% of cells were dead after incubation with H/GM@MSN (**Figure 3**d), which was in line with the results of the CCK-8 study. These results were evidence of the synergistic effect of CDT and autophagy-inhibitory treatment enhanced the cell toxicity. Additionally, cell apoptosis rates were further investigated by flow cytometry (**Figure 3**e). The induction rate of H/GM@MSN on necrotic/late apoptotic cells was 19.6% while other groups showed lower ratios of apoptotic cells, which was aligned with the results from CCK-8 and live/dead assays.

It has been shown that CDT therapy based on Mn^{2+} can also induce ICD of tumor cells. [44] Meanwhile, the released Mn^{2+} can activate the STING pathway, and thus increase the rate of maturation of the DCs and recruit T killer cells. Calreticulin (CRT), which mediates the “eat me” signaling, directs DCs to gobble up dying tumor cells, and high mobility group box 1 (HMGB1), an ICD-associated immunogenicity biomarker, can also promote DC maturation and antigen presentation. [45,46] CRT exposure of 4T1 cells was evaluated with flow cytometry.

The H/GM@MSN group showed the highest expression level of CRT (F=211.2) among the PBS, LipHCQ, M@MSN, and GM@MSN groups (**Figure 3**f). In addition, an immunofluorescence staining assay also verified the expression of CRT, which showed a dramatic increment in the GM@MSN and H/GM@MSN groups, in accordance with flow cytometry results (**Figure 3**g). The H/GM@MSN group released 116 ng/mL of HMGB1, which was 1.28-fold and 2.68-fold times than that in the GM@MSN and M@MSN groups (**Figure S17**). The maturation of DCs was verified by the double positivity of CD80 and CD86 costimulatory molecules, which was considered as a marker of DC maturation.[47] **Figures 3**h and i show that the DC maturity rates were 26.5%, 33.1%, 42.7%, and 49.8% for the PBS, M@MSN, GM@MSN, and H/GM@MSN groups, respectively. On the one hand, CDT could cause the release of more tumor antigens to induce ICD and stimulate DC maturation. On the other hand, CDT based on Mn^{2+} and the braking effect of LipHCQ enhanced STING activation, resulting in the increased release of IFN-β. Further stimulation of DC maturation activated the antitumor immune response and regulated the TME. These results showed that the combination of CDT, Mn^{2+} release, and autophagy inhibition could amplify STING signaling, promote DC maturation effectively, and enhance the intracellular antitumor immunotherapy effect.

3.4. Activation of the STING pathway and inhibition of autophagy by NPs *in vitro*

It has shown that the innate immune system is activated when cGAS binds to cytoplasmic DNA.[48] **Figure 4**a illustrates the process of DC activation via ROS-triggered release of dsDNA fragments from tumor cells and subsequent activated the STING pathway. Expression of STING, TBK1, IRF3, phosphorylated STING (P-STING, Ser366), phosphorylated TBK1 (P-TBK1, Ser172) and phosphorylated IRF3 (P-IRF3, Ser396) were assessed by western blot, which reflected the activation effect of GM@MSN combined with LipHCQ on the STING pathway. As a result, the expression of P-STING, P-TBK1 and P-IRF3 were significantly higher in the M@MSN, and H/GM@MSN groups compared to other groups (**Figure 4**b, **S18**). In addition, to evaluate the effect of H/GM@MSN on the STING pathway, the release of INF-β (**Figure 4**c), IL-6 (**Figure 4**d) and TNF-α(**Figure 4**e) was evaluated by ELISA. H/GM@MSN group showed the most release of induction-related factors, which confirmed that CDT combined with Mn^{2+} release could amplify the STING signal and induce Active Ingredient and inflammatory factors released by 4T1 cells. The addition of LipHCQ together with Mn^{2+} could cause stronger STING activation.

Tumor cells also activated their internal protective autophagy in response to counter the excess ROS and weakened the activation effect of the STING pathway (**Figure 4**f). [30] To better understand the activation of STING, autophagy levels were also explored after the treatment. The expression of LC3B-II and SQSTM1/p62 (p62) were assessed by western blot. The LC3B-II and p62 proteins in LipHCQ-treated cells were significantly increased (**Figure 4**g, **S19**), indicating that intracellular autophagosomes were abundantly produced due to autophagy inhibition compared to the PBS group and GM@MSN group. In addition, p62 proteins in GM@MSN-treated cells were downregulated, which could be attributed to protective autophagy due to activation of the STING pathway. Importantly, the LC3B-II and p62 expression in the H/GM@MSN group were higher than in other groups, indicating that the process of internal protective autophagy could be largely inhibited (F=18.28). Blockage of this

pathway should be conducive to the enhancement of oxidative damage and the accumulation of dsDNA, which further amplifies the STING pathway. In addition, the autophagic flux of cells with different treatments was visually tracked by Bio-TEM. As shown in **Figure 4**h, cells treated with GM@MSN produced more autophagosomes than the PBS group, indicating that protective autophagy occurred when STING was enhanced by CDT. Remarkably, the number of autophagic vesicles in the H/GM@MSN group was greatly increased compared to that in the GM@MSN group, which further suggested that autophagy inhibition effectively promoted the damage-associated cellular components caused by excess ROS, thereby exacerbating oxidative damage. The introduction of HCQ eliminates intracellular negative feedback regulation, which is expected to contribute to the enhancement of oxidative damage induced by CDT.

3.5. Inhibition of tumor recurrence and metastatic tumor growth *in vivo*

The *in vivo* fate of drugs was examined by evaluating the distributions of Cy5.5-lablled GM@MSN in major organs (*i.e.*, heart, liver, spleen, lung, kidney and tumor). After 2 and 5 days injection, GM@MSN were mainly accumulated in the tumor, indicating their effective targeted delivery ability (**Figure S20**). 4T1-bearing tumor models were used for the detection of tumor recurrence inhibitory activity after surgery, the schedule of which was shown in **Figure 5**a. The remaining area after tumor resection was determined using MR imaging. (**Figure S21, Table 1**). The tumor resection cavity was injected with different formulas, including PBS solution, LipHCQ-loaded hydrogel (H@Gel), M@MSN-loaded hydrogel (M@Gel), GM@MSN-loaded hydrogel (GM@Gel), and H/GM@Gel before suturing. The body weight and tumor volume were monitored every 3 days. Between groups, no significant weight loss was observed (**Figure 5**b). The tumor volume was monitored with vernier calipers (**Figure 5**c). The tumor volume in the PBS, H@Gel, and M@Gel groups increased over 1000 mm^3 after 15-day post-injection. The tumors in the GM@Gel group had a tendency to increase in the later stage, which could be related to the immunosuppressive tumor microenvironment and lack of tumor-associated antigens.[49] In contrast, mice treated with H/GM@Gel could significantly suppress the tumor recurrence, indicating that gel-mediated GOx combined with Mn^{2+} and autophagy inhibitor had strong antitumor ability. The weights and photographs of the tumors removed after different treatments confirmed the antitumor efficacy of H/GM@Gel over the other groups (F=51.21) (**Figure 5**d**,** e). In addition, we also examined the level of ROS production *in vivo* and found that the H/GM@Gel group resulted in higher levels than the PBS group, which was also consistent with the treatment outcomes. **(Figure S22)**

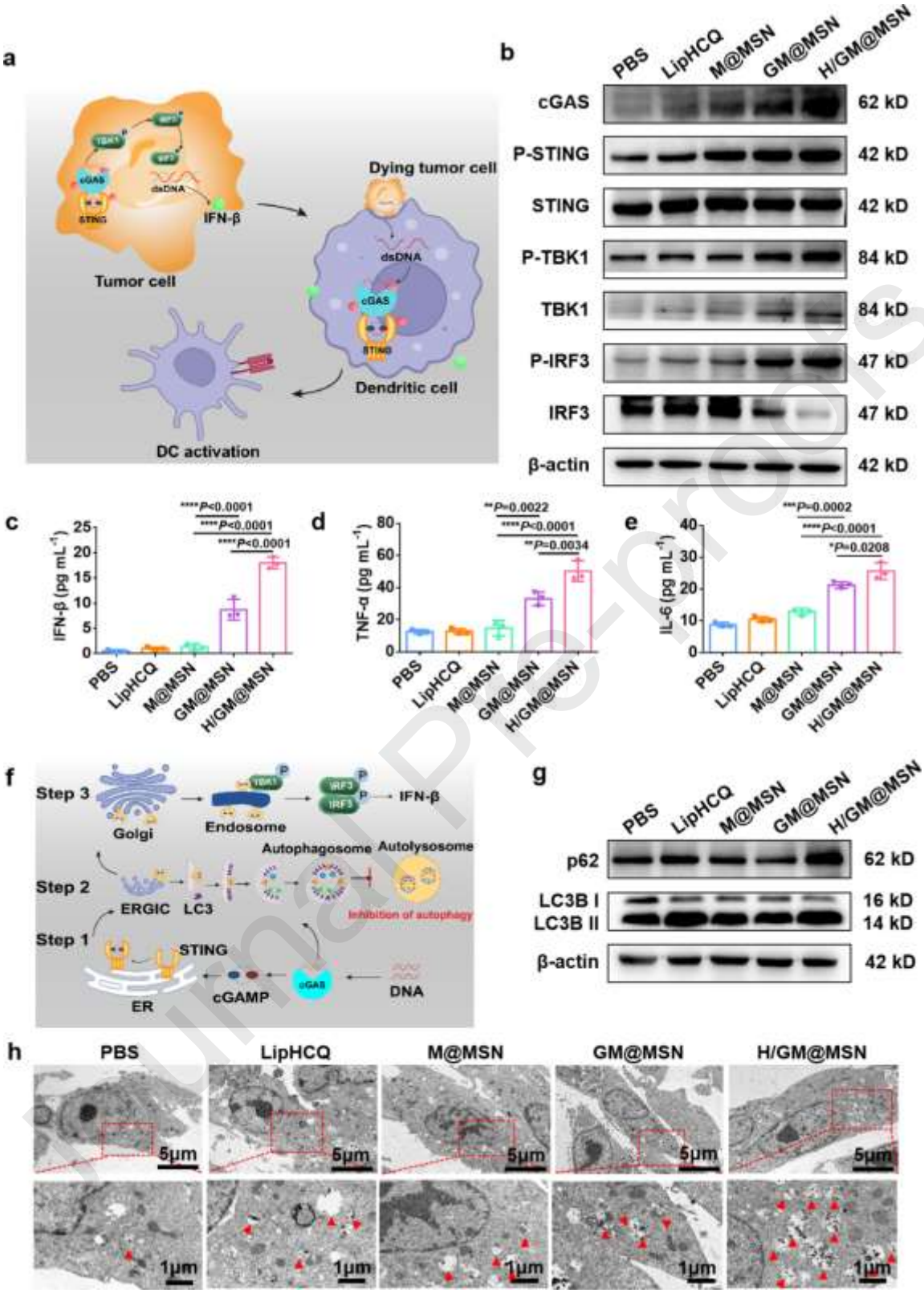

Figure 4. Evaluation of the effect of amplifying the STING pathway. a) Scheme showing the activation of the STING pathway. b) Western blot analysis of STING pathway proteins after incubation of 4T1 cells with PBS, LipHCQ, M@MSN, GM@MSN or H/GM@MSN. Secretion of c) IFN-β, d) TNF-α, e) IL-6 characterized by ELISA. f) Schematic showing the HCQ enhanced STING pathway. g) Expression of the autophagy indicator proteins (*i.e.*, LC3B and

SQSTM1/p62) in 4T1 cells after 24 h incubation with different NPs. h) Bio-TEM images of autolysosomes in 4T1 cells with different treatments for 24 h. Significant differences were assessed using one-way ANOVA. Data are presented as the mean ± SD (n=3). *$P < 0.05$, **$P < 0.01$, ***$P < 0.001$, ****$P < 0.0001$.

Histological analysis was performed to evaluate the tumor-inhibitory effect. Hematoxylin-eosin (H&E) staining images showed obvious cell necrosis and apoptosis in both the GM@Gel group and H/GM@Gel group (**Figure 5**f). As observed from the Ki67 tumor staining images, only a few staining signals of tumor cells were detected in the H/GM@Gel group (**Figure 5**f), which further verified that GOx combined with Mn^{2+} and autophagy inhibition had an excellent antitumor effect. The main organs (*i.e.*, lung, liver, spleen, kidney and heart) of mice were obtained and stained by H&E. No obvious tissue necrosis was observed in either treatment group (**Figure S23**). The blood biochemical results (ALT, alanine aminotransferase; ALP, alkaline phosphatase; BUN, blood urea nitrogen; CREA, creatinine) between the PBS group and other groups treated with the hydrogel-immobilized NPs were not significantly different (**Figure S24**). The above results demonstrate the safety of hydrogel-immobilized NPs and their transformation feasibility.

Given the strong antitumor effect of the H/GM@Gel hydrogel-immobilized NPs, H/GM@Gel is expected to be promising for the inhibition of metastatic tumor growth. To evaluate the efficacy of H/GM@Gel inhibition of metastatic tumor growth, a lung metastasis model was established (**Figure 5**g). Survival curves for the mice showed that the H/GM@Gel hydrogels significantly prolonged the survival time of mice (**Figure 5**h). Lung tissues were collected to determine the extent of metastasis. The H/GM@Gel group had much less lung metastatic nodules than the other groups (**Figure 5**i), which indicated that lung metastatic tumor growth effectively inhibited by H/GM@Gel (F=62.5) (**Figure 5**j). In addition, the H&E staining results were in accordance with the results of lung metastatic nodules (**Figure 5**k). Overall, H/GM@Gel showed good ability to inhibit the metastatic tumors growth, attributed to its high level of systemic antitumor immunity.

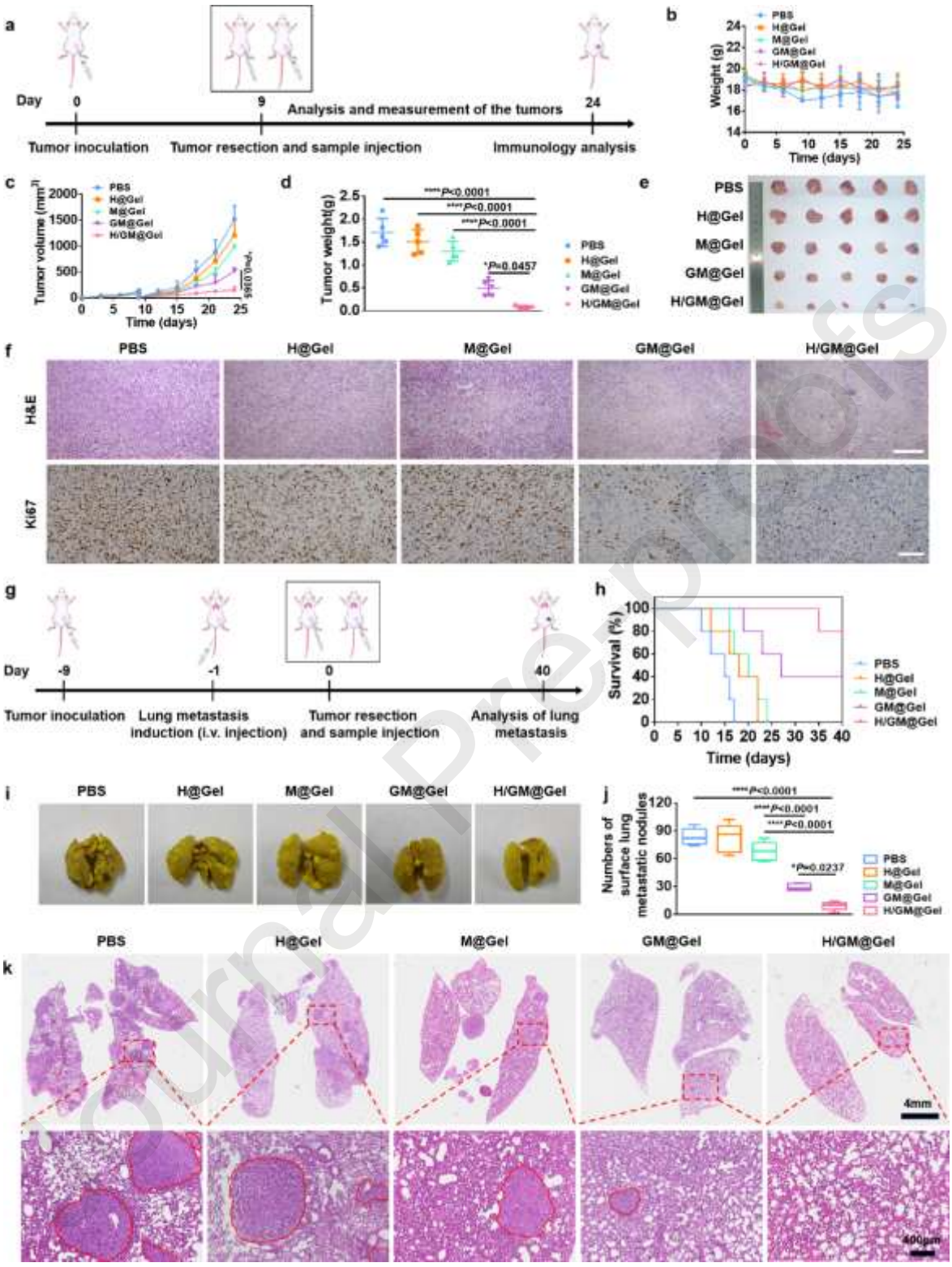

Figure 5. *In vivo* evaluation of immunotherapy with H/GM@Gel in mouse models of recurrence and lung metastasis. a) Schematic diagram of immunotherapy based on the inhibition of tumor recurrence. b) Changes in body weight of mice during treatment. c) Tumor volume changes d) and tumor weight after treatments with PBS, H@Gel, M@Gel, GM@Gel, and H/GM@Gel (GOx: 3 mg/kg; HCQ:10 mg/kg). e) Photographs of the recurrent tumors after different treatments. f) H&E and Ki67 staining images of recurrence tumor tissue with different

treatments. Scale bar is 200 μm. g) Illustration of immunotherapy based on the inhibition of lung metastatic tumor. h) Growth curves of tumors after the different treatments. i) Photographs, j) analysis, and k) Metastatic lung nodules with different treatments in H&E staining. Scale bars are 4 mm and 400 μm. Significant differences were assessed using one-way ANOVA. Data are presented as the mean ± SD (n=5). *$P < 0.05$, ****$P < 0.0001$.

3.6. Synergistic antitumor mechanism of the hydrogel-immobilized NPs

To explore the mechanism of synergistic antitumor effects, the immune responses in tumor tissues and lymph nodes (LNs) were investigated. Compared with the other groups, the H/GM@Gel group had the highest DC maturation rate (5.1% and 7.6%) in both LNs and tumors **(Figure 6**a-d), indicating that CDT-induced ICD could stimulate DC maturation in the TME. Following the trend of DC maturation, the abundance of $CD8^+$ T cells and $CD4^+$ T cells was significantly higher in the H/GM@Gel group than that in the other groups, which was because mature DCs released more inflammatory mediators capable of triggering immune responses. Among them, H/GM@Gel significantly promoted $CD8^+$ T cells (11.9%, $P < 0.0001$) in comparison with the PBS group (3.6%), and the proportion of $CD8^+$ T cells in the H/GM@Gel group was approximately 1.4 times higher than in the GM@Gel group (F=21.39). **(Figure 6**e, f), which was due to synergy between autophagy inhibition and STING activation. In other words, CDT significantly enhanced the activation of the STING pathway by Mn^{2+}, and HCQ relieved the "brake" signal on the STING pathway, which resulted in the secretion of more IFN-β and proinflammatory cytokines to stimulate DC maturation and subsequently recruit more cytotoxic T lymphocytes (CTLs). In addition, the ratio of $CD4^+$ T cells, which are capable of assisting and maintaining the CTL response, in the H/GM@Gel group (5.1%) was also the highest among the treatment groups (F=12.74) **(Figures 6**g, **S25**). These results confirmed that enhanced STING pathway activation combined with autophagy inhibition significantly activated the antitumor immune responses.

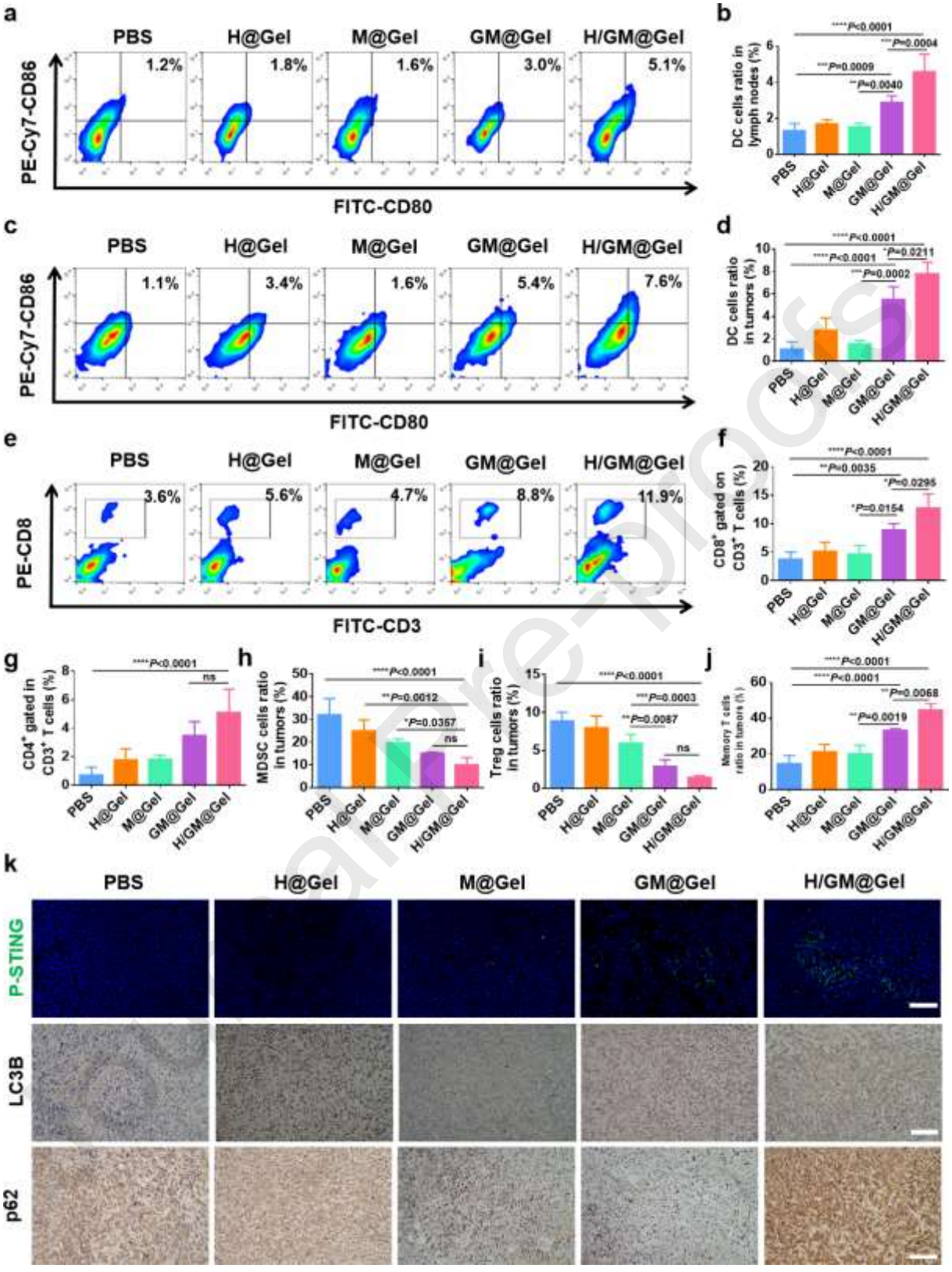

Figure 6. *In vivo* alterations in the TME after various treatments. a-d) Flow cytometry results of DC maturation in lymph nodes (a, b) and tumor tissues (c, d) after different treatments (n = 5). e, f) Proportions of $CD8^+$ T cells in tumors after different treatments with PBS, H@Gel, M@Gel, GM@Gel, and H/GM@Gel. Percentages of $CD3^+$ $CD4^+$, g), $CD45^+CD11b^+$ $Gr1^+$, h),

$CD4^+$ CD25 $Foxp3^+$, i) and $CD62L^-$ $CD44^+$j) T cells in total T cells in 4T1 tumors after different treatments. k) Immunofluorescence images of P-STING and immunohistochemistry images of LC3B and p62 proteins in different recurrent tumor groups. Scale bars are 200 μm. ***P < 0.001, ****P < 0.0001.

To assess the ability of NPs to reverse the immunosuppressive tumor microenvironment, the ratios of myeloid-derived suppressor cells (MDSCs, $CD45^+Gr1^+CD11b^+$) and immunosuppressive regulatory T cells (Tregs, $CD4^+CD25^+Foxp3^+$) were examined by flow cytometry. As show in **Figures 6**h and **S26,** the proportion of MDSCs was significantly reduced in the H/GM@Gel group (7.3%) in comparison with the PBS group (37.6%), thus alleviating the immunosuppressive effect of MDSC on CTLs and enhancing the immunotherapeutic effect (F=16.47). Since Tregs can inhibit the potent antitumor immune response to CTLs, the frequency of Tregs in the TME was investigated. **Figures 6**i and **S27** show that the H/GM@Gel group significantly decreased the proportion of Tregs (1.4%) (F=35.28). These results indicated that the H/GM@Gel could also alleviate the immunosuppressive TME. As is well known memory T cells ($CD3^+CD8^+CD62L^-CD44^+$) are essential to provide rapid protection against pathogen reinfection and tumor recurrence. Due to the good therapeutic effect of H/GM@Gel in inhibiting recurrence and metastatic tumor growth, the ratio of effector memory T cells within the TME was examined. The H/GM@Gel treatment group (43.3%) produced significantly higher memory T cells levels than the PBS treatment group (18.3%) (F=39) (**Figures 6**j and **S28**). It indicated that H/GM@Gel could effectively enhance antitumor immunotherapy responses and promote long-acting immune memory effects to prevent tumor recurrence and metastatic tumor growth.

The immunofluorescence staining was also performed in tumor tissue to examine the expression of $CD8^+$ T and $CD4^+$ T cells. More fluorescence signals were found in the H/GM@Gel group, indicating that H/GM@Gel could improve levels of tumor infiltration in $CD8^+$ T and $CD4^+$ T cells, which was consistent with the results from flow cytometry (**Figure S29**). Furthermore, the tumor sections were also stained with P-STING (Ser366), cGAS and P-IRF3 (Ser396) proteins to investigate the antitumor effect of H/GM@Gel *via* fluorescence microscopy. The group treated with H/GM@Gel showed high expression of P-STING (Ser366) protein as well as cGAS and P-IRF3 (Ser396) proteins, which indicates that the activation of the STING pathway can effectively inhibit tumor growth (**Figure 6**k, **Figure S30**). Immunohistochemical analysis of the autophagy protein markers LC3B and p62 in tumor sections showed that the expression of both proteins increased after H/GM@Gel treatment, suggesting that the autophagy process was significantly inhibited and autophagy lysosomes were degraded (**Figure 6**k). These immunohistochemical results are consistent with the data at the cellular level. Mn^{2+} and GOx-based CDT initiated oxidative stress, thus activating STING pathway, while the protective autophagy generated was inhibited by HCQ. As a result, the two synergies enhanced the cGAS-STING pathway and aggravate oxidative damage. Simultaneously, suppressing the innate detoxification effect of cancer cells through autophagy inhibition ultimately leads to tumor regression.

4. Conclusion

Activation of the STING pathway is essential to effectively exert antitumor immunity. H/GM@Gel therapeutic platform was designed to effectively generate ROS in tumor tissues *via* CDT, which could accelerate and amplify the activation of the STING pathway in combination with Mn^{2+} to enhance innate immunity. In addition, HCQ could inhibit the protective autophagy induced by STING pathway activation and further amplify the antitumor immune responses. Meanwhile, CDT effectively induced ICD, released tumor cell antigens, stimulated DC maturation, and recruited more T cells for tumor cell killing. As a result, H/GM@Gel demonstrated superior STING pathway activation in tumors. Potent activation of the STING pathway promoted the release of IFN-β and the recruitment of antigen-specific T cells, thereby significantly inhibiting tumor recurrence and metastatic tumor growth after surgery. In summary, STING agonist loaded with autophagy inhibitor exerted potent antitumor effects in the 4T1 tumor-bearing mouse model, which provides a prospective transformation method for biomedical applications in postsurgical tumor therapy.

Declaration of Competing Interest

The authors declare that they have no known competing financial interests or personal relationships that could have appeared to influence the work reported in this paper.

Acknowledgements

This work was supported by the National Natural Science Foundation of China (22102088, 22072075, 81771888, 82202228); Innovation Project of Jinan Science and Technology Bureau (2020GXRC022); and Natural Science Foundation of Shandong Province of China (ZR2021QB046, ZR2017MH006). This work was performed in part at the Analytical Centre for Structural Constituent and Physical Property, and the Translational Medicine Core Facility of Advanced Medical Research Institute at Shandong University.

Supporting Information

Supplementary data to this article can be found online at

Reference

[1] H. Pan, R. Gray, J. Braybrooke, C. Davies, C. Taylor, P. McGale, R. Peto, K.I. Pritchard, J. Bergh, M. Dowsett, D.F. Hayes, EBCTCG, 20-Year Risks of Breast-Cancer Recurrence after Stopping Endocrine Therapy at 5 Years, N. Engl. J. Med. 377 (2017) 1836-1846. https://doi.org/10.1056/NEJMoa1701830.

[2] F. Borri, A. Granaglia, Pathology of triple negative breast cancer, Semin. Cancer Biol. 72 (2021) 136-145. https://doi.org/10.1016/j.semcancer.2020.06.005.

[3] P. Mehlen, A. Puisieux, Metastasis: a question of life or death, Nat. Rev. Cancer 6 (2006) 449-458. https://doi.org/10.1038/nrc1886.

[4] A.C. Begg, F.A. Stewart, C. Vens, Strategies to improve radiotherapy with targeted drugs, Nat. Rev. Cancer 11 (2011) 239-253. https://doi.org/10.1038/nrc3007.

[5] R.A. Leon-Ferre, M.P. Goetz, Advances in systemic therapies for triple negative breast cancer, BMJ 381 (2023) e071674. https://doi.org/10.1136/bmj-2022-071674.

[6] O. Saatci, A. Kaymak, U. Raza, P.G. Ersan, O. Akbulut, C.E. Banister, V. Sikirzhytski, U.M. Tokat, G. Aykut, S.A. Ansari, H.T. Dogan, M. Dogan, P. Jandaghi, A. Isik, F. Gundogdu, K. Kosemehmetoglu, O. Dizdar, S. Aksoy, A. Akyol, A. Uner, P.J. Buckhaults, Y. Riazalhosseini, O. Sahin, Targeting lysyl oxidase (LOX) overcomes chemotherapy resistance in triple negative breast cancer, Nat. Commun. 11 (2020) 2416. https:// doi.org/ 10.1038/s41467-020-16199-4.

[7] J. Conde, N. Oliva, Y. Zhang, N. Artzi, Local triple-combination therapy results in tumour regression and prevents recurrence in a colon cancer model, Nat. Mater. 15 (2016) 1128-1138. https://doi.org/10.1038/nmat4707.

[8] Y. Zhang, Z. Feng, J. Liu, H. Li, Q. Su, J. Zhang, P. Huang, W. Wang, J. Liu, Polarization of tumor-associated macrophages by TLR7/8 conjugated radiosensitive peptide hydrogel for overcoming tumor radioresistance, Bioact. Mater. 16 (2022) 359-371. https://doi.org/10.1016/j.bioactmat.2021.12.033.

[9] P. Savas, B. Virassamy, C. Ye, A. Salim, C.P. Mintoff, F. Caramia, R. Salgado, D.J. Byrne, Z.L. Teo, S. Dushyanthen, A. Byrne, L. Wein, S.J. Luen, C. Poliness, S.S. Nightingale, A.S. Skandarajah, D.E. Gyorki, C.M. Thornton, P.A. Beavis, S.B. Fox, Kathleen Cuningham Foundation Consortium for Research into Familial Breast Cancer (kConFab), P.K. Darcy, T.P. Speed, L.K. Mackay, P.J. Neeson, S. Loi, Single-cell profiling of breast cancer T cells reveals a tissue-resident memory subset associated with improved prognosis, Nat. Med. 24 (2018) 986-993. https://doi.org/10.1038/s41591-018-0078-7.

[10] Q. Chen, C. Wang, X. Zhang, G. Chen, Q. Hu, H. Li, J. Wang, D. Wen, Y. Zhang, Y. Lu, G. Yang, C. Jiang, J. Wang, G. Dotti, Z. Gu, In situ sprayed bioresponsive

immunotherapeutic gel for post-surgical cancer treatment, Nat. Nanotechnol. 14 (2019) 89-97. https://doi.org/10.1038/s41565-018-0319-4.

[11] C. Wang, W. Sun, Y. Ye, Q. Hu, H.N. Bomba, Z. Gu, In situ activation of platelets with checkpoint inhibitors for post-surgical cancer immunotherapy, Nat. Biomed. Eng. 1 (2017) 0011. https://doi.org/10.1038/s41551-016-0011.

[12] N.L. Syn, M.W.L. Teng, T.S.K. Mok, R.A. Soo, De-novo and acquired resistance to immune checkpoint targeting, Lancet Oncol. 18 (2017) e731–e741. https://doi.org/ 10.1016/S1470-2045(17)30607-1.

[13] H. Phuengkham, C. Song, Y.T. Lim, A Designer Scaffold with Immune Nanoconverters for Reverting Immunosuppression and Enhancing Immune Checkpoint Blockade Therapy, Adv. Mater. 31 (2019) e1903242. https://doi.org/10.1002/adma.201903242.

[14] T. Wang, H. Zhang, W. Qiu, Y. Han, H. Liu, Z. Li, Biomimetic nanoparticles directly remodel immunosuppressive microenvironment for boosting glioblastoma immunotherapy, Bioact. Mater. 16 (2022) 418–432. https://doi.org/ 10.1016/ j.bioactmat. 2021.12.029.

[15] L. Huang, Y. Zhang, Y. Li, F. Meng, H. Li, H. Zhang, J. Tu, C. Sun, L. Luo, Time-Programmed Delivery of Active Ingredient and Anti-CD47 Antibody via a Double-Layer-Gel Matrix for Postsurgical Treatment of Breast Cancer, Nano-Micro Lett. 13 (2021) 141. https://doi.org/10.1007/s40820-021-00647-x.

[16] Yang M., Li J., Gu P., Fan X. The application of nanoparticles in cancer immunotherapy: targeting tumor microenvironment, Bioact. Mater. 6 (2021) 1973-1987.10.1016/j. bioactmat.2020.12.010. https://doi.org/10.1016/j.bioactmat.2020.12.010.

[17] W. Guo, Z. Chen, Z. Li, H. Huang, Y. Ren, B. Zhao, G. Li, Y. Hu, Improved immunotherapy for gastric cancer by nanocomposites with capability of triggering Dual-Damage of Nuclear/Mitochondrial DNA and cGAS/STING-Mediated innate immunity, Chem. Eng. J. 443 (2022) 136428. https://doi.org/10.1016/ j.cej. 2022. 136428.

[18] D. Shae, K.W. Becker, P. Christov, D.S. Yun, A.K.R. Lytton-Jean, S. Sevimli, M. Ascano, M. Kelley, D.B. Johnson, J.M. Balko, J.T. Wilson, Endosomolytic polymersomes increase the activity of cyclic dinucleotide STING agonists to enhance cancer immunotherapy, Nat. Nanotechnol. 14 (2019) 269–278. https://doi.org/ 10.1038/ s41565-018-0342-5.

[19] J. Cai, S. Jiang, J. Liao, H. Fan, C. Peng, S. Shi, S. Huang, G. Chen, J. Xu, Z. Wang, Manganese-doped biostimulatory nanoneedle for MRI-visual bispecific antibody gene delivery and immunosuppression reversal as a cancer immunotherapy strategy, Chem. Eng. J. 462 (2023) 142242. https://doi.org/10.1016/j.cej.2023.142242.

[20] J. Guo, L. Huang, Nanodelivery of cGAS-STING activators for tumor immunotherapy, Trends Pharmacol. Sci. 43 (2022) 957–972. https://doi.org/10.1016/j.tips.2022.08.006.

[21] M. Wang, X. Zhang, B. Liu, C. Liu, C. Song, Y. Chen, Y. Jin, J. Lin, P. Huang, S. Xing, Immunotherapeutic Hydrogel with Photothermal Induced Immunogenic Cell Death and STING Activation for Post-Surgical Treatment, Adv. Funct. Mater. 33 (2023) 2300199. https://doi.org/10.1002/adfm.202300199.

[22] S. Glück, B. Guey, M.F. Gulen, K. Wolter, T.-W. Kang, N.A. Schmacke, A. Bridgeman, J. Rehwinkel, L. Zender, A. Ablasser, Innate immune sensing of cytosolic chromatin fragments through cGAS promotes senescence, Nat. Cell Biol. 19 (2017) 1061–1070. https://doi.org/10.1038/ncb3586.

[23] M. He, T. Xiao, Y. Wang, H. Yu, Z. Wang, X. Shi, H. Wang, Multifunctional PVCL nanogels enable magnetic resonance imaging and immunostimulated radiotherapy of orthotopic glioblastoma, Chem. Eng. J. 453 (2023) 139634. https://doi.org/ 10.1016/j.cej. 2022.139634.

[24] C. Wang, Y. Guan, M. Lv, R. Zhang, Z. Guo, X. Wei, X. Du, J. Yang, T. Li, Y. Wan, X. Su, X. Huang, Z. Jiang, Manganese Increases the Sensitivity of the cGAS-STING Pathway for Double-Stranded DNA and Is Required for the Host Defense against DNA Viruses, Immunity 48 (2018) 675-687.e7. https://doi.org/10.1016/j.immuni.2018.03.017.

[25] Z. Zhao, Z. Ma, B. Wang, Y. Guan, X.-D. Su, Z. Jiang, Mn2+ Directly Activates cGAS and Structural Analysis Suggests Mn2+ Induces a Noncanonical Catalytic Synthesis of 2’3’-cGAMP, Cell Rep. 32 (2020) 108053. https://doi.org/10.1016/j.celrep.2020.108053.

[26] Y. Zhu, Z. Yang, Z. Pan, Y. Hao, C. Wang, Z. Dong, Q. Li, Y. Han, L. Tian, L. Feng, Z. Liu, Metallo-alginate hydrogel can potentiate microwave tumor ablation for synergistic cancer treatment, Sci. Adv. 8 (2022) eabo5285. https://doi.org/10.1126/sciadv.abo5285.

[27] J. Yan, G. Wang, L. Xie, H. Tian, J. Li, B. Li, W. Sang, W. Li, Z. Zhang, Y. Dai, Engineering Radiosensitizer-Based Metal-Phenolic Networks Potentiate STING Pathway Activation for Advanced Radiotherapy, Adv. Mater. 34 (2022) e2105783. https://doi.org/10.1002/adma.202105783.

[28] M. Lv, M. Chen, R. Zhang, W. Zhang, C. Wang, Y. Zhang, X. Wei, Y. Guan, J. Liu, K. Feng, M. Jing, X. Wang, Y.-C. Liu, Q. Mei, W. Han, Z. Jiang, Manganese is critical for antitumor immune responses via cGAS-STING and improves the efficacy of clinical immunotherapy, Cell Res. 30 (2020) 966-979. https://doi.org/10.1038/s41422-020-00395-4.

[29] J. Yang, X. Tang, K.S. Nandakumar, K. Cheng, Autophagy induced by STING, an unnoticed and primordial function of cGAS, Cell. Mol. Immunol. 16 (2019) 683–684. https://doi.org/10.1038/s41423-019-0240-2.

[30] D. Liu, H. Wu, C. Wang, Y. Li, H. Tian, S. Siraj, S.A. Sehgal, X. Wang, J. Wang, Y. Shang, Z. Jiang, L. Liu, Q. Chen, STING directly activates autophagy to tune the innate

immune response, Cell Death Differ. 26 (2019) 1735–1749. https://doi.org/ 10.1038/ s41418-018-0251-z.

[31] Z. Yang, D.J. Klionsky, Eaten alive: a history of macroautophagy, Nat. Cell Biol. 12 (2010) 814–822. https://doi.org/10.1038/ncb0910-814.

[32] W. Guo, Z. Chen, Z. Li, H. Huang, Y. Ren, B. Zhao, G. Li, Y. Hu, Improved immunotherapy for gastric cancer by nanocomposites with capability of triggering Dual-Damage of Nuclear/Mitochondrial DNA and cGAS/STING-Mediated innate immunity, Chem. Eng. J. 443 (2022) 136428. https://doi.org/10.1016/j.cej.2022. 136428.

[33] H. Wu, F. Wu, T. Zhou, Z. Hu, W. Wang, X. Liang, J. Wang, C. You, B. Sun, F. Lin, Activatable autophagy inhibition-primed chemodynamic therapy via targeted sandwich-like two-dimensional nanosheets, Chem. Eng. J. 431 (2021) 133470. https://doi.org/ 10.1016/j.cej.2021.133470.

[34] B. Yang, L. Ding, H. Yao, Y. Chen, J. Shi, A metal-organic framework (MOF) Fenton nanoagent-enabled nanocatalytic cancer therapy in synergy with autophagy inhibition, Adv. Mater. 32 (2020) 1907152. https://doi.org/ 10.1002/adma.201907152.

[35] M. Chen, D. Yang, Y. Sun, T. Liu, W. Wang, J. Fu, Q. Wang, X. Bai, G. Quan, X. Pan, C. Wu, In situ self-assembly nanomicelle microneedles for enhanced photoimmunotherapy via autophagy regulation strategy, ACS Nano 15 (2021) 3387–3401. https://doi.org/10.1021/acsnano.0c10396.

[36] X. Gui, H. Yang, T. Li, X. Tan, P. Shi, M. Li, F. Du, Z.J. Chen, Autophagy induction via STING trafficking is a primordial function of the cGAS pathway, Nature 567 (2019) 262–266. https://doi.org/10.1038/s41586-019-1006-9.

[37] L. Li, Z. Yang, W. Fan, L. He, C. Cui, J. Zou, W. Tang, O. Jacobson, Z. Wang, G. Niu, S. Hu, X. Chen, In Situ Polymerized Hollow Mesoporous Organosilica Biocatalysis Nanoreactor for Enhancing ROS-Mediated Anticancer Therapy, Adv. Funct. Mater. 30 (2020) 1907716. https://doi.org/10.1002/adfm.201907716.

[38] L. Cao, H. Tian, M. Fang, Z. Xu, D. Tang, J. Chen, J. Yin, H. Xiao, K. Shang, H. Han, X. Li, Activating cGAS-STING pathway with ROS-responsive nanoparticles delivering a hybrid prodrug for enhanced chemo-immunotherapy, Biomaterials 290 (2022) 121856. https://doi.org/10.1016/j.biomaterials.2022.121856.

[39] Y. Rao, G. Xu, Z. Zhang, W. Wang, C. Zhang, M. Zhao, Y. Qu, W. Li, M. Ji, Y. Liu, Y.-Q. Li, Coupling doping and localized surface plasmon resonance toward acidic pHpreferential catalase-like nanozyme for oxygen-dominated synergistic cancer therapy, Chem. Eng. J. 465 (2023).

[40] S. Zhang, Y. Zhang, Y. Feng, J. Wu, Y. Hu, L. Lin, C. Xu, J. Chen, Z. Tang, H. Tian, X. Chen, Biomineralized Two-Enzyme Nanoparticles Regulate Tumor Glycometabolism

Inducing Tumor Cell Pyroptosis and Robust Antitumor Immunotherapy, Adv. Mater. 34 (2022) e2206851. https://doi.org/10.1002/adma.202206851.

[41] L.-H. Fu, Y.-R. Hu, C. Qi, T. He, S. Jiang, C. Jiang, J. He, J. Qu, J. Lin, P. Huang, Biodegradable Manganese-Doped Calcium Phosphate Nanotheranostics for Traceable Cascade Reaction-Enhanced Anti-Tumor Therapy, ACS Nano 13 (2019) 13985–13994. https://doi.org/10.1021/acsnano.9b05836.

[42] Q. He, R. Zheng, J. Ma, L. Zhao, Y. Shi, J. Qiu, Responsive manganese-based nanoplatform amplifying cGAS-STING activation for immunotherapy, Biomater. Res. 27 (2023) 29. https://doi.org/10.1186/s40824-023-00374-x.

[43] Y. Zhao, Y. Pan, K. Zou, Z. Lan, G. Cheng, Q. Mai, H. Cui, Q. Meng, T. Chen, L. Rao, L. Ma, G. Yu, Biomimetic manganese-based theranostic nanoplatform for cancer multimodal imaging and twofold immunotherapy, Bioact. Mater. 19 (2023) 237–250. https://doi.org/10.1016/j.bioactmat.2022.04.011.

[44] X. Zhao, K. Guo, K. Zhang, S. Duan, M. Chen, N. Zhao, F.-J. Xu, Orchestrated Yolk-Shell Nanohybrids Regulate Macrophage Polarization and Dendritic Cell Maturation for Oncotherapy with Augmented Antitumor Immunity, Adv. Mater. 34 (2022) e2108263. https://doi.org/10.1002/adma.202108263.

[45] B. Feng, Z. Niu, B. Hou, L. Zhou, Y. Li, H. Yu, Enhancing Triple Negative Breast Cancer Immunotherapy by ICG-Templated Self-Assembly of Active Ingredient Nanoparticles, Adv. Funct. Mater. 30 (2020) 1906605. https://doi.org/10.1002/adfm.201906605.

[46] Q. Chen, J. Chen, Z. Yang, J. Xu, L. Xu, C. Liang, X. Han, Z. Liu, Nanoparticle-Enhanced Radiotherapy to Trigger Robust Cancer Immunotherapy, Adv. Mater. 31 (2019) 1802228. https://doi.org/10.1002/adma.201802228.

[47] W. Yang, G. Zhu, S. Wang, G. Yu, Z. Yang, L. Lin, Z. Zhou, Y. Liu, Y. Dai, F. Zhang, Z. Shen, Y. Liu, Z. He, J. Lau, G. Niu, D.O. Kiesewetter, S. Hu, X. Chen, In Situ Dendritic Cell Vaccine for Effective Cancer Immunotherapy, ACS Nano 13 (2019) 3083–3094. https://doi.org/10.1021/acsnano.8b08346.

[48] H. Liu, H. Zhang, X. Wu, D. Ma, J. Wu, L. Wang, Y. Jiang, Y. Fei, C. Zhu, R. Tan, P. Jungblut, G. Pei, A. Dorhoi, Q. Yan, F. Zhang, R. Zheng, S. Liu, H. Liang, Z. Liu, H. Yang, J. Chen, P. Wang, T. Tang, W. Peng, Z. Hu, Z. Xu, X. Huang, J. Wang, H. Li, Y. Zhou, F. Liu, D. Yan, S.H.E. Kaufmann, C. Chen, Z. Mao, B. Ge, Nuclear cGAS suppresses DNA repair and promotes tumorigenesis, Nature 563 (2018) 131–136. https://doi.org/10.1038/s41586-018-0629-6.

[49] H. Liu, B. Kwong, D.J. Irvine, Membrane anchored immunostimulatory oligonucleotides for in vivo cell modification and localized immunotherapy, Angew. Chem., Int. Ed. 50 (2011) 7052–7055. https://doi.org/10.1002/anie.201101266.

706

707 **Declaration of Competing Interest**

708 The authors declare that they have no known competing financial interests or personal
709 relationships that could have appeared to influence the work reported in this paper.

710

711 ## Highlights

712 - Hydrogel-immobilized NPs applied for sustained drug release

713 - Activation of protective autophagy induce the amplification of the STING pathway

714 - CDT-IMT can inhibit tumor recurrence and metastatic tumor growth

715